

High-resolution optical spectroscopy and modeling of spectral and magnetic properties of multiferroic $\text{ErFe}_3(\text{BO}_3)_4$

M. N. Popova ^{1,*}, E. P. Chukalina,¹ D. S. Erofeev ¹, A. Jablunovskis ², I. A. Gudim ³, and B. Z. Malkin ⁴

¹*Institute of Spectroscopy, Russian Academy of Sciences, 108840 Troitsk, Moscow, Russia*

²*Moscow Institute of Physics and Technology (National Research University), 141701 Dolgoprudny, Moscow region, Russia*

³*L. V. Kirensky Institute of Physics, Siberian Branch of RAS, 660036, Krasnoyarsk, Russia*

⁴*Kazan Federal University, 420008 Kazan, Russia*



(Received 8 March 2020; accepted 9 April 2020; published 7 May 2020)

We carried out the high-resolution broadband temperature-dependent polarized optical spectroscopy and theoretical studies of $\text{ErFe}_3(\text{BO}_3)_4$ single crystals in the paramagnetic and antiferromagnetic ($T < T_N = 39$ K) phases. On the basis of the experimentally determined 45 crystal-field (CF) levels of Er^{3+} ions at sites with the C_2 point symmetry, CF calculations were performed, a set of physically grounded CF parameters was obtained and used to model the temperature dependences of the Er magnetic moments measured in neutron-scattering experiments, as well as the magnetic susceptibility and magnetization of the compound; the contributions of the quasi-one-dimensional iron magnetic subsystem were calculated in the frame of the previously developed self-consistent four-particle cluster model. The modeling strongly supports an easy-plane collinear structure of iron magnetic moments and excludes earlier proposed additional magnetic phase.

DOI: [10.1103/PhysRevB.101.205108](https://doi.org/10.1103/PhysRevB.101.205108)

I. INTRODUCTION

Erbium iron borate $\text{ErFe}_3(\text{BO}_3)_4$ belongs to the family of rare-earth (RE) iron borates $R\text{Fe}_3(\text{BO}_3)_4$ ($R = \text{La}, \text{Pr}, \text{Er}, \text{Y}$), which has recently attracted considerable attention due to interesting magnetic and magnetoelectric properties. The presence of two interacting magnetic subsystems (the Fe and RE ones) stimulate a wide variety of magnetic phases, in particular, when the easy-plane magnetic anisotropy of the S -state iron ions Fe^{3+} competes with the easy-axis anisotropy of RE ions. What is even more important, some of RE iron borates demonstrate a considerable magnetoelectric effect. Thus, a quadratic magnetoelectric effect registered in $\text{TbFe}_3(\text{BO}_3)_4$ at room temperature in the magnetic field applied along the a axis exceeded the one observed in the high-temperature multiferroic BiFeO_3 . The sign of the effect changed upon rotation of the magnetic field by 90° around the c axis, which is attractive for applications [1].

Depending on a particular R^{3+} ion, RE iron borates possess strongly different magnetic, magnetoelectric, magnetoelastic (e.g., Refs. [2–5] and references therein), and magnetodielectric [5–8] properties. Anisotropy of the R^{3+} ion promotes either an easy-axis ($R = \text{Pr}, \text{Gd}, \text{Tb}, \text{Dy}$) or an easy-plane ($R = \text{Nd}, \text{Sm}, \text{Eu}, \text{Ho}, \text{Er}, \text{Y}$) magnetic structure of $R\text{Fe}_3(\text{BO}_3)_4$ below the antiferromagnetic ordering temperature $T_N \sim 30 - 40$ K [9]. In particular, $\text{ErFe}_3(\text{BO}_3)_4$ orders magnetically at $T_N = 39$ K into an easy-plane structure [10,11]. While the easy-axis iron borates demonstrate a weak magnetic-field-induced electric polarization, $P \sim 10 \mu\text{C}/\text{m}^2$, an order of magnitude greater values were observed in

the easy-plane ones ($P = 80, 400, \text{ and } 500 \mu\text{C}/\text{m}^2$ for Eu, Nd, and Sm iron borates, respectively [3]). Unexpectedly, a negligible effect ($P < 1 \mu\text{C}/\text{m}^2$) was recorded for the easy-plane magnet $\text{ErFe}_3(\text{BO}_3)_4$ [3]. To understand the physics of magnetoelectricity in RE iron borates, it is necessary to develop a microscopic theory of magnetoelectric interactions. This can be done on the basis of a detailed knowledge of crystal and magnetic structures, physically justified crystal-field (CF) and electron-deformation interaction parameters for the RE ions, and the parameters of the Fe-RE exchange interactions [12,13].

RE iron borates crystallize in the $R32$ space-symmetry group and have the structure of the natural mineral huntite [14–16]. In this structure, FeO_6 octahedra share common edges forming isolated helical chains along the trigonal c axis. The chains are interconnected by BO_3 triangles and isolated RO_6 distorted prisms characterized by the D_3 point-symmetry group. Whereas $R\text{Fe}_3(\text{BO}_3)_4$ with “big” R^{3+} ions ($R = \text{La}, \text{Pr}, \text{Nd}, \text{ and } \text{Sm}$) possess the $R32$ structure in the whole range of temperatures, those with $R = \text{Eu} - \text{Er}, \text{Y}$ undergo a weak first-order $R32 \rightarrow P3_121(P3_221)$ structural phase transition, the temperature T_S of which linearly grows with diminishing the ionic radius of R^{3+} and reaches 427 K for $\text{HoFe}_3(\text{BO}_3)_4$, according to data on powder samples prepared by solid-phase synthesis [2]. No data exist on T_S for so synthesized $\text{ErFe}_3(\text{BO}_3)_4$ but the approximation of the dependence of T_S on the ionic radius of the RE ion [2] provides a value of about 500 K. Single crystals of RE iron borates are produced by solution-melt technique with different fluxes [14], and the first large crystals of good optical quality were grown in the laboratory of Bezmaternykh in the Kirensky Institute of Physics, Krasnoyarsk, using a $\text{Bi}_2\text{Mo}_3\text{O}_{12}$ -based flux [17]. Early $\text{ErFe}_3(\text{BO}_3)_4$ single crystals demonstrated $T_S \sim 340$ K

*popova@isan.troitsk.ru

(Raman measurements [18]) whereas later samples obtained with improved solution-melt technology showed $T_S = 433$ K at cooling and 439 K at heating (heat capacity measurements [19]). It is worth noting that erbium iron borate is the last compound in the series of RE iron borates, which was managed to grow as a single crystal, and it is especially important to choose the optimal crystal-growth conditions for getting crystals of good optical quality. However, even the best single crystals of RE iron borates grown by solution-melt technique with the Bi-containing flux have lower T_S than powder samples prepared by solid-phase synthesis. It was explained by “big” Bi^{3+} ions that enter into positions of the “small” RE^{3+} ions from the flux in the course of the crystal growth and increase the effective radius of ions in the RE sublattice [20,16]. In any case, at room temperature and below, the title compound has the low-symmetry structure corresponding to the enantiomorphic space-group pair $P3_121$ (D_3^4 , No. 152) and $P3_221$ (D_3^6 , No. 154). For both members of the pair, symmetry of the Er site lowers from D_3 to C_2 [15,16,18]. Domains of left-handed $P3_221$ and right-handed $P3_121$ helical structures of ErO_6 distorted prisms and FeO_6 octahedra can exist in $\text{ErFe}_3(\text{BO}_3)_4$ crystals, in the same way as in $\text{DyFe}_3(\text{BO}_3)_4$ [21] (see also Fig. 1 in Ref. [22]).

In our previous studies, we have derived CF parameters for the Nd [23], Sm [24], Pr [25], Tb [26], Eu [20], and Dy [22] iron borates, starting from an initial set of parameters calculated in the framework of the exchange-charge model [27] and using an experimental set of CF levels obtained from an analysis of the high-resolution optical spectra. We also registered the spectral changes in the magnetically ordered state and used these data to evaluate the exchange-interaction parameters. These and CF parameters obtained on the basis of high-resolution spectroscopic data were used to model magnetic susceptibilities [20,22–26] and magnetoelectric responses [12,13,20] of the RE iron borates.

In this paper, we report such procedure for $\text{ErFe}_3(\text{BO}_3)_4$. We perform thorough high-resolution broadband polarized temperature-dependent optical absorption measurements of the $\text{ErFe}_3(\text{BO}_3)_4$ single crystals in the paramagnetic and antiferromagnetic phases and, analyzing the spectra, construct the corresponding energy-level schemes. The CF and exchange-interaction parameters obtained on that basis are further used to model magnetic properties of the compound. This simulation elucidates details of the low-temperature magnetic structure of $\text{ErFe}_3(\text{BO}_3)_4$. We are not aware of any attempts to find the CF and exchange-interaction parameters of Er^{3+} ions in $\text{ErFe}_3(\text{BO}_3)_4$ on the basis of spectroscopic results. High-resolution spectra in a broad spectral and temperature range of a sample in the paramagnetic and magnetically ordered states are necessary for that. As far as we know, there are no such data in the literature. In Refs. [19,28], the σ - and π -polarized absorption and magnetic circular dichroism spectra of f - f transitions in $\text{ErFe}_3(\text{BO}_3)_4$ single crystals were registered only at temperatures ≥ 90 K in the range from 9500 (spectral resolution 4 cm^{-1}) to $22\,000 \text{ cm}^{-1}$ (spectral resolution 10 cm^{-1}) using a grating spectrometer with not well-calibrated wave-number scale (the latter point is addressed in Sec. III A). This resulted in a wrong assignment of many spectral lines, wrong energy values of erbium CF levels, and not justified conclusions concerning the energies

of local vibrations and changes of the local symmetry of the Er^{3+} ion in optically excited states.

The paper is organized as follows. In Sec. II, we describe the samples used and the details of optical measurements. Section III reports the high-resolution temperature-dependent polarized optical spectra of $\text{ErFe}_3(\text{BO}_3)_4$. Section IV is devoted to a theoretical consideration. The paper ends with Summary.

II. EXPERIMENTAL DETAILS

The $\text{ErFe}_3(\text{BO}_3)_4$ single crystals were grown by solution-melt technique [29] using the $\text{Bi}_2\text{Mo}_3\text{O}_{12}$ -based flux: 76.7 wt. % ($\text{Bi}_2\text{Mo}_3\text{O}_{12} + 3.14\text{B}_2\text{O}_3 + 0.54\text{Er}_2\text{O}_3$) + 23.3 wt. % $\text{ErFe}_3(\text{BO}_3)_4$. The saturation temperature of such solution melt was found to be $T_{\text{sat}} = 945 \pm 3^\circ\text{C}$. First of all, crystals of about 1 mm^3 in size were obtained at the spontaneous crystallization regime at the temperature $T = T_{\text{sat}} - 20^\circ\text{C}$. They were used as seeds to grow the crystals of about $5 \times 7 \times 7 \text{ mm}^3$ in size, with the rate not exceeding 1 mm/day . More details on the crystal growth can be found in Ref. [29]. The crystals of good optical quality were oriented using their morphology and optical polarization methods. Samples for optical measurements were cut either perpendicular or parallel to the c axis and polished to the thickness $d = 0.117 \text{ mm}$.

Transmission spectra of the erbium iron borate were registered in a spectral range $5000 - 23000 \text{ cm}^{-1}$ with the resolution of 0.2 cm^{-1} using a Fourier spectrometer Bruker IFS 125 HR. It should be noted that an accurate scale of wave numbers in the entire spectral range is an inherent property of Fourier transform spectroscopy, where a stabilized laser is used for calibration. For measurements in the temperature range $4 - 300$ K, a closed helium-cycle cryostat Cryomech ST403 was used. At $T < 70 \text{ K}$ ($T > 70 \text{ K}$), the temperature was stabilized with the precision $\pm 0.05 \text{ K}$ ($\pm 0.1 \text{ K}$). A heating attachment Bruker 2216e was used for the temperature range $300 - 450 \text{ K}$. We

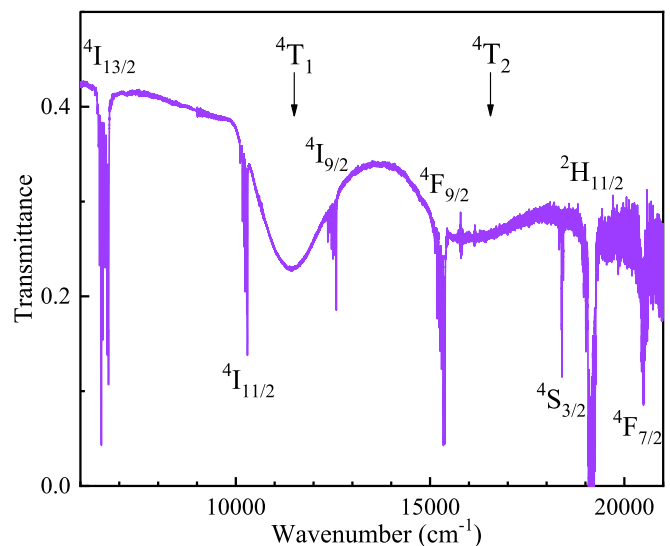


FIG. 1. Broadband transmission spectrum of a $\text{ErFe}_3(\text{BO}_3)_4$ single crystal at 50 K. The final states of the Er^{3+} (Fe^{3+}) transitions from the ground state $^4I_{15/2}$ (6A_1) are indicated.

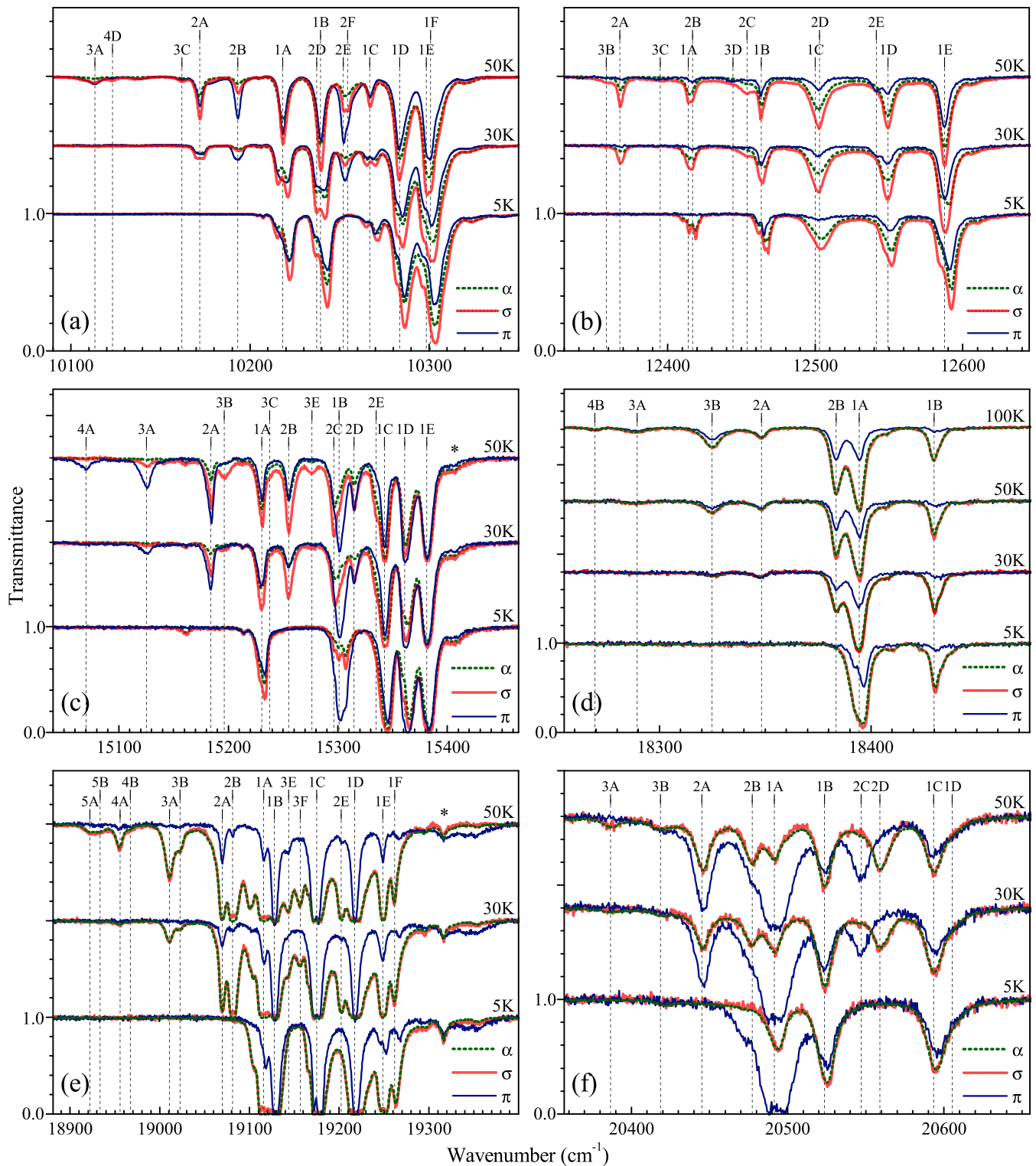


FIG. 2. The α -, σ -, and π -polarized transmission spectra of an $\text{ErFe}_3(\text{BO}_3)_4$ single crystal in the region of optical transitions from the ground multiplet $^4I_{15/2}$ to the excited multiplets (a) $^4I_{11/2}$, (b) $^4I_{9/2}$, (c) $^4F_{9/2}$, (d) $^4S_{3/2}$, (e) $^2H_{11/2}$, and (f) $^4F_{7/2}$ at the temperatures below $T_S \approx 433$ K (i.e., in the $P3_121$ phase): 100 K [in (d) only], $50 \text{ K} > T_N = 39 \text{ K}$ and 30 K , $5 \text{ K} < T_N$ after subtraction of the appropriate spectra of $\text{GdFe}_3(\text{BO}_3)_4$. The spectra at 30, 50, and 100 K are vertically shifted. Stars (*) mark absorption lines of some impurities.

TABLE I. Experimental and calculated (with CF parameters presented in Table II) energies of CF levels of the Er^{3+} ions in paramagnetic $\text{ErFe}_3(\text{BO}_3)_4$ ($T = 50$ K). Δ_1 and Δ_2 denote the exchange splittings of Kramers doublets of magnetically nonequivalent Er1 and Er2 (see the text), respectively, at $T = 5$ K (all values are in cm^{-1}).

$2S+1L_J$		E (exper.)	E (calc.)	Δ_1 (calc.)	Δ_2 (calc.)
1	2	3	4	5	
$4I_{15/2}$	1	0	0	5.25	6.21
	2	46.3	46.25	1.28	0.73
	3	105	105.8	4.51	3.89
	4	160.4	139.0	2.30	1.74
	5	194	159.9	3.65	1.93
	6	244	232.6	0.85	4.78
	7	279.2	275.3	2.07	3.87
	8	296.4	294.4	3.81	3.99
$4I_{13/2}$	A	6539.3	6539.8	2.44	3.15
	B	6572.9	6573.1	0.46	0.49
	C	6622.6	6616.7	1.84	1.45
	D	6638.5	6628.8	1.18	0.99
	E	6684.4	6682	0.20	2.63
	F	6714.3	6713.7	1.43	1.39
	G	6722.5	6725.5	1.82	1.82
$4I_{11/2}$	A	10 218.3	10 218	0.07	0.12
	B	10 239.4	10 241	0.02	0.05
	C	10 267	10 268	0.00	0.03
	D	10 283.5	10 288	0.02	0.25
	E	10 298.4	10 309	0.12	0.15
	F	10 300.8	10 316	0.29	0.23
	G	12 414.1	12 431	1.20	2.00
$4I_{9/2}$	A	12 414.1	12 431	1.20	2.00
	B	12 463.4	12 465	0.82	0.43
	C	12 500	12 497	0.98	1.16
	D	12 549.3	12 550	0.42	0.35
	E	12 587.6	12 600	1.31	1.24
	F	15 230.5	15 233	0.12	0.28
	G	15 301.3	15 295	3.06	2.27
$4F_{9/2}$	A	15 342.6	15 333	0.26	1.21
	B	15 361	15 354	0.12	0.98
	C	15 381.3	15 382	0.14	2.08
	D	15 394.5	18 395	1.43	1.86
	E	18 429.9	18 430	3.93	5.92
	F	19 115.9	19 117	0.54	0.79
	G	19 127.5	19 126	2.02	1.49
$2H_{11/2}$	A	19 127.5	19 126	2.02	1.49
	B	19 174.8	19 170	1.79	1.46
	C	19 217.2	19 216	1.17	1.02
	D	19 248.5	19 241	3.98	2.57
	E	19 261.7	19 258	0.06	0.13
	F	20 491.5	20 492	2.03	2.27
	G	20 523.5	20 530	2.20	1.65
$4F_{7/2}$	A	20 523.5	20 530	2.20	1.65
	B	20 593.4	20 583	2.27	2.58
	C	20 605.3	20 598	0.85	4.03
	D	22 180	22 183	0.00	0.27
$4F_{5/2}$	A	22 180	22 183	0.00	0.27
	B	22 202	22 198	0.18	0.31
	C	22 239	22 230	1.16	1.13

employed either unpolarized light propagating along the c axis of the crystal ($\mathbf{k}||c$, $\mathbf{E}\perp c$, $\mathbf{H}\perp c$: α polarization) or linearly polarized light incident perpendicular to the c axis ($\mathbf{k}\perp c$, $\mathbf{E}\perp c$, $\mathbf{H}||c$: σ polarization; $\mathbf{k}||c$, $\mathbf{E}||c$, $\mathbf{H}\perp c$: π polarization).

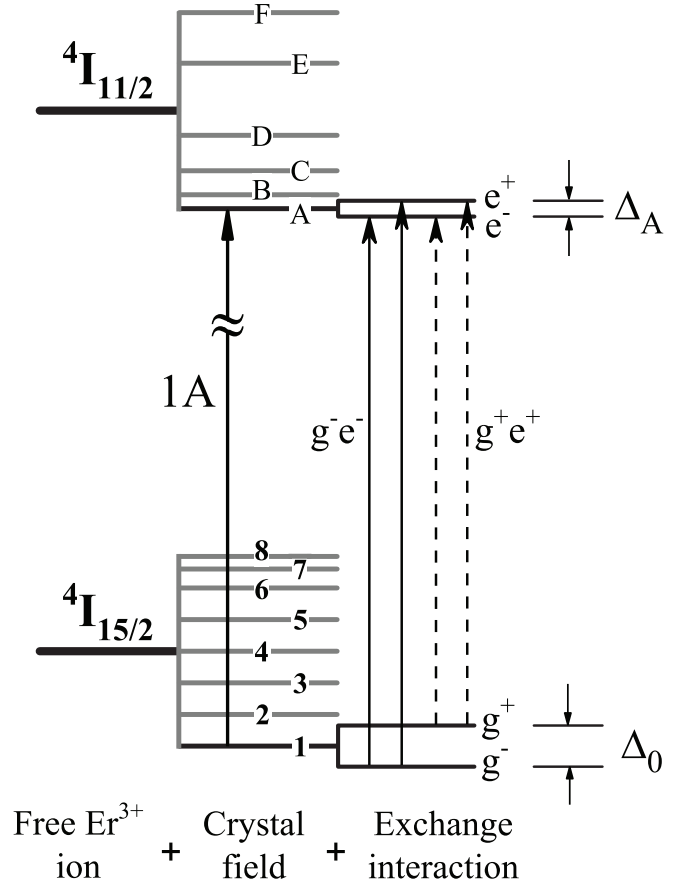


FIG. 3. Scheme of levels and optical transitions of the Er^{3+} ion in a magnetic crystal.

III. OPTICAL SPECTRA OF $\text{ErFe}_3(\text{BO}_3)_4$

A. Paramagnetic $\text{ErFe}_3(\text{BO}_3)_4$ in the $P3_121$ ($P3_221$) phase: Crystal-field levels

Figure 1 demonstrates a transmission spectrum of $\text{ErFe}_3(\text{BO}_3)_4$ in the whole spectral region studied. Two wide bands designated $4T_1$ and $4T_2$ correspond to $d-d$ optical transitions between the ground ($6A_1$) and excited states (with the total spin $S = 3/2$) of the $3d^5$ electronic shell of the Fe^{3+} ions. These are the absorption bands of iron ions that determine the green color of iron borate single crystals. Intensive absorption in the region of wave numbers above $24\,000\text{ cm}^{-1}$ is connected with charge-transfer transitions [30]. Numerous narrow spectral lines are due to the $f-f$ optical transitions between the energy levels of the $4f^{11}$ electronic shell of the Er^{3+} ions. After subtracting the $d-d$ absorption bands [e.g., measured in $\text{GdFe}_3(\text{BO}_3)_4$ where $f-f$ transitions start at energies above $\sim 30\,000\text{ cm}^{-1}$], one gets the spectra of the $f-f$ transitions.

Figure 2 shows thus obtained polarized spectra for several optical multiplets of Er^{3+} in the low-symmetry $P3_121$ ($P3_221$) phase of $\text{ErFe}_3(\text{BO}_3)_4$ at different temperatures, both above (100 and 50 K) and below (30 and 5 K) the temperature $T_N = 39$ K of a magnetic ordering. The levels of a free Er^{3+} ion (which has an odd number of electrons and, thus, is a Kramers ion), characterized by the total momentum J , in the crystal field of C_2 symmetry at erbium sites in $\text{ErFe}_3(\text{BO}_3)_4$

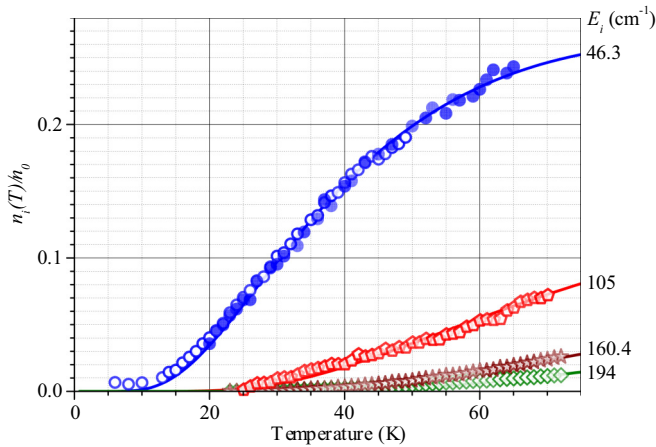


FIG. 4. Calculated (solid lines) relative populations $n_i(T)/n_0$ of the excited levels (n_i is the number of Er^{3+} ions at the i th level with the energy E_i , n_0 is the total number of Er^{3+} ions) and experimentally measured integral intensities of spectral lines (symbols). Open circles, disks, pentagons, stars, and diamonds represent the data for the lines 10 172, 18 348, 18 325, 18 956, and 18 922 cm^{-1} , respectively.

split into $J + 1/2$ Kramers doublets. A detailed study of the temperature dependences of the line positions and intensities allowed us to identify the spectral lines and to find the energies of CF levels of Er^{3+} in the paramagnetic $\text{ErFe}_3(\text{BO}_3)_4$. They are listed in Table I for $T = 50$ K.

In this paper, notations of spectral lines contain the initial and final levels of optical transitions. CF levels of a given excited multiplet and the sublevels of the ground multiplet $^4I_{15/2}$ are labeled by capital letters (A, B, etc.) and the numbers 1, 2...8 in order of increasing energy, respectively (see the scheme of Fig. 3). Some of spectral lines disappear with decreasing the temperature [e.g., 4A, 3A, 2A, 2B, etc. in Fig. 2(c)]. Evidently, these lines begin at excited sublevels of the ground multiplet, the populations of which diminish with lowering the temperature. Their intensities follow the Boltzmann distribution of the levels' populations (see Fig. 4).

At the lowest temperature of 5 K, only the ground level is populated, and well-resolved lines corresponding to optical transitions from the ground state to the CF sublevels of excited multiplets are observed (see Fig. 2). In some cases, positions of CF levels could be determined only with the help of transitions from the excited levels of the ground multiplet [see, e.g., Fig. 2(f) for the $^4I_{15/2} \rightarrow ^4F_{7/2}$ transition, where the line 1D is hidden in the wing of the line 1C but the clearly observed line 2D helps to precisely find the position of 1D]. Temperature-dependent transmission spectra of the $^4I_{15/2} \rightarrow ^4I_{13/2}$ transition, as well as the CF levels of the $^4I_{13/2}$ multiplet, were given in Ref. [31]. Energies of the CF levels 4–8 of the ground multiplet $^4I_{15/2}$ were specified using the spectra of a thicker sample ($d = 2.016$ mm) [31].

To illustrate how important for correct lines' identification is to analyze the spectra at $T < 90$ K, we take as an example the simplest transition $^4I_{15/2} \rightarrow ^4S_{3/2}$ shown in Fig. 2(d) at 100, 50, 30, and 5 K and in Fig. 5 of Ref. [28] at 90 K. The $^4S_{3/2}$ CF manifold consists of only two levels, they are unambiguously identified from the absorption (transmission) spectra at 5 K (lines 1A and 1B). With increasing the temperature, lines originating from the excited CF levels 2, 3, etc. of the ground

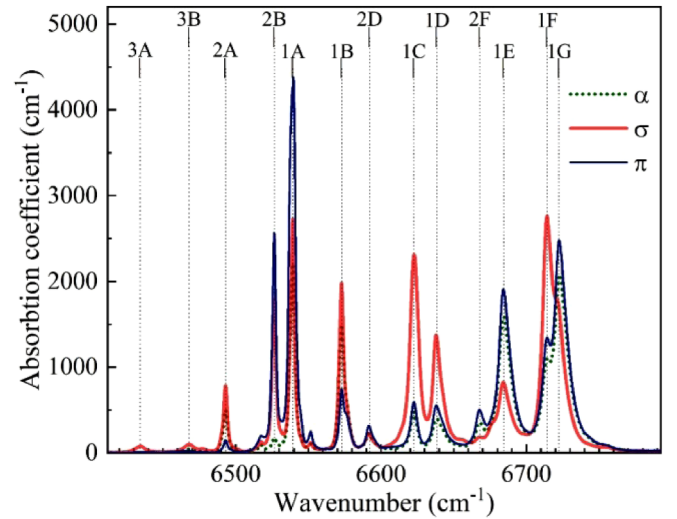


FIG. 5. Absorption spectrum of $\text{ErFe}_3(\text{BO}_3)_4$ in the region of the $^4I_{15/2} \rightarrow ^4I_{13/2}$ transition. $T = 50$ K. Lines in the high-frequency part (> 6600 cm^{-1}) of the transition coincide in α and π polarizations, which testifies their purely magnetic dipole origin.

$^4I_{15/2}$ manifold appear (2A, 2B, 3A, 3B, etc.), their intensities follow the Boltzmann distribution of the levels' populations (see Fig. 4). In Ref. [28], where the spectra were registered at $T \geq 90$ K, wrong assignments of the spectral lines were given, namely, the lines 3B and 2B + 1A were attributed to the transitions from the ground state, with a splitting of the high-frequency component due to a local distortion in the excited state; the line 1B was interpreted as a vibronic satellite of the line 3B. We also remark that the wave-number scale in Fig. 5 of Ref. [28] is shifted by ~ 70 cm^{-1} , which follows from a comparison with the spectra registered at a Fourier spectrometer [Fig. 2(d)] where a stabilized laser is used for calibration of the entire wave-number scale.

We note that most of the spectral lines presented in Fig. 2 coincide in the α and σ polarizations, which testifies their electric dipole nature. On the contrary, many spectral lines of the $^4I_{15/2} \rightarrow ^4I_{13/2}$ transition, which is allowed as magnetic dipole in a free Er^{3+} ion, coincide in the α and π polarizations demonstrating purely magnetic dipole origin. Absorption spectrum of the $^4I_{15/2} \rightarrow ^4I_{13/2}$ transition shown in Fig. 5 illustrates this.

Having in hand a set of 45 excited CF levels of Er^{3+} in $\text{ErFe}_3(\text{BO}_3)_4$, we perform CF calculations in Sec. IV.

B. Splitting of the erbium Kramers doublets in a magnetically ordered state of $\text{ErFe}_3(\text{BO}_3)_4$

At the temperatures below the Néel temperature $T_N = 39$ K, the erbium spectral lines split, following the splitting of Kramers doublets due to exchange interaction of the Er^{3+} ions with an ordered iron magnetic subsystem (see the scheme of Fig. 3). Figure 6(a) displays the line 1A of the $^4I_{15/2} \rightarrow ^4I_{11/2}$ transition at $T = 45$ K $> T_N$ and at several temperatures below T_N . The line splitting is clearly observed and the low-frequency part of the split line decreases in intensity with lowering the temperature, because of diminishing the population of the upper component g^+ of the split ground Kramers

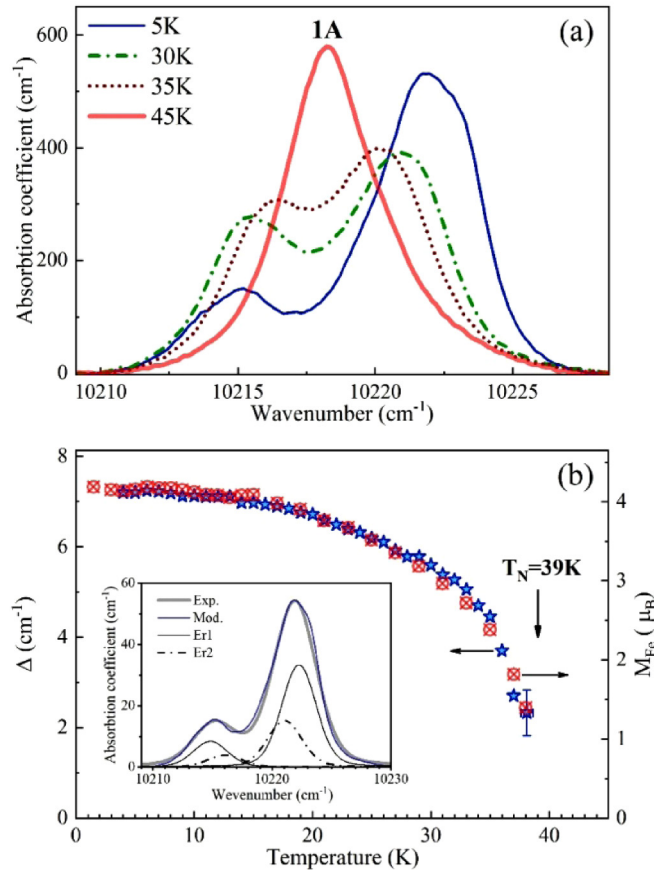


FIG. 6. Splitting Δ of the line 1A in the ${}^4I_{15/2} \rightarrow {}^4I_{11/2}$ optical multiplet of $\text{ErFe}_3(\text{BO}_3)_4$. (a) absorption spectra at several temperatures, (b) the $\Delta(T)$ dependence (blue stars) compared with the $M_{\text{Fe}}(T)$ dependence (red circles with a cross) from neutron-scattering measurements [11]. Inset shows decomposition of the line at 5 K into Voigt components (see the text).

doublet (see Fig. 3). Figure 6(b) presents the temperature dependences of the line splitting $\Delta(T)$ and of the Fe^{3+} magnetic moment $M_{\text{Fe}}(T)$ measured in neutron-scattering experiments [11]. A perfect proportionality between $\Delta(T)$ and $M_{\text{Fe}}(T)$ is evident. Two conclusions can be drawn from this fact, namely (1) Kramers doublets of erbium split due to the Er-Fe interaction, the Er-Er interaction being much weaker; (2) splitting of spectral lines $\Delta(T)$ can be considered as an order parameter of the magnetic phase transition. Dominance of the RE-Fe interactions over the RE-RE ones has been confirmed earlier for other RE iron borates [20,22–26].

The shape of the split spectral lines will be discussed in Sec. IV D after the calculation of exchange splitting of the Er^{3+} Kramers doublets in a magnetically ordered state of $\text{ErFe}_3(\text{BO}_3)_4$.

IV. SIMULATIONS OF SPECTRAL AND MAGNETIC PROPERTIES

A. Crystal-field calculations for paramagnetic $\text{ErFe}_3(\text{BO}_3)_4$ in the $P3_121$ phase

The electronic structure of Er^{3+} ions of even erbium isotopes (natural abundance 75.6%) in the crystal field of C_2 symmetry in erbium iron borate is determined by the standard

single-ion Hamiltonian acting in the full basis of 364 states of the $4f^{11}$ electronic shell,

$$H = H_{\text{FI}} + H_{\text{CF}} + H_Z, \quad (1)$$

where H_{FI} is the parametrized free-ion Hamiltonian [32],

$$\begin{aligned} H_{\text{FI}} = & \sum_{k=2,4,6} F^k \hat{f}_k + \zeta \sum_j \mathbf{I}_j s_j + \alpha \left(\sum_j \mathbf{I}_j \right)^2 + \beta \hat{G}(G_2) \\ & + \gamma \hat{G}(R_7) + \sum_{k=2,3,4,6,7,8} T^k \hat{t}_k + \sum_{k=0,2,4} M^k \hat{m}_k \\ & + \sum_{k=2,4,6} P^k \hat{p}_k. \end{aligned} \quad (2)$$

The H_{CF} operator represents the energy of 4f electrons in a crystal field, in the Cartesian coordinate system with the z and x axes along the crystallographic axes c and a , respectively,

$$\begin{aligned} H_{\text{CF}} = & B_0^2 C_0^{(2)} + B_0^4 C_0^{(4)} + B_0^6 C_0^{(6)} + iB_{-3}^4 (C_{-3}^{(4)} + C_3^{(4)}) \\ & + iB_{-3}^6 (C_{-3}^{(6)} + C_3^{(6)}) + B_6^6 (C_{-6}^{(6)} + C_6^{(6)}) \\ & + i[B_{-1}^2 (C_{-1}^{(2)} + C_1^{(2)}) + B_{-1}^4 (C_{-1}^{(4)} + C_1^{(4)}) \\ & + B_{-1}^6 (C_{-1}^{(6)} + C_1^{(6)}) + B_{-5}^6 (C_{-5}^{(6)} + C_5^{(6)})] \\ & + B_2^2 (C_{-2}^{(2)} + C_2^{(2)}) + B_2^4 (C_{-2}^{(4)} + C_2^{(4)}) \\ & + B_2^6 (C_{-2}^{(6)} + C_2^{(6)}) + B_4^4 (C_{-4}^{(4)} + C_4^{(4)}) \\ & + B_4^6 (C_{-4}^{(6)} + C_4^{(6)}), \end{aligned} \quad (3)$$

and H_Z is the ion energy in a local magnetic field \mathbf{B}_{loc} ,

$$H_Z = \sum_j \mu_B (k \mathbf{I}_j + 2s_j) \mathbf{B}_{\text{loc}} \quad (4)$$

(here k is the orbital reduction factor). The 4f electrons are labeled above by the index j , the explicit expressions for operators \hat{f} , \hat{t} , \hat{m} , \hat{p} and the Casimir operators $\hat{G}(G_2)$ and $\hat{G}(R_7)$ can be found in the literature (see Ref. [32]), $C_q^{(p)} = \sum_j C_{q,j}^{(p)}$; $C_{q,j}^{(p)}$, \mathbf{I}_j , and s_j are single-electron spherical tensor, orbital moment, and spin moment operators, respectively. Matrices of all electronic operators in the Hamiltonian (1) were computed in the basis of 364 Slater determinants for the $4f^{11}$ electronic shell. Next, similarly to some previous studies of spectral properties of Er^{3+} ions in crystals [33,34], matrix elements of the fourth-rank spherical tensor operators $C_q^{(4)}$ within the ${}^2H_{11/2}$ and ${}^4I_{9/2}$ manifolds were corrected by the factors of 1.4 and 0.9, respectively. The fitting procedure for the CF energies of Er^{3+} ions determined from optical data in the paramagnetic phase of $\text{ErFe}_3(\text{BO}_3)_4$ involved numerical diagonalization of the Hamiltonian (1) for $\mathbf{B}_{\text{loc}} = 0$ and varied sets of CF parameters B_q^p and parameters of the free-ion Hamiltonian (2). The initial values of the free-ion parameters were taken from Ref. [35] [namely, the parameters for the impurity Er^{3+} ions in $\text{YAl}_3(\text{BO}_3)_4$ with the $R32$ crystal structure], the most of these parameters, except the parameters F^k of electrostatic two-electron interactions, were kept fixed or only slightly changed. The final set of the free-ion parameters in units of cm^{-1} used in the present work is the following: $F^2 = 96\,800$ (96 329), $F^4 = 67\,980$ (68 001), $F^6 = 54\,170$ (53 342), the

TABLE II. Crystal-field parameters B_q^p (cm^{-1}) for RE iron borates with the $P3_121$ structure. In the $P3_221$ structure, the parameters with $q = -1, -3$, and -5 have opposite signs.

p	q	EuFe ₃ (BO ₃) ₄	TbFe ₃ (BO ₃) ₄	DyFe ₃ (BO ₃) ₄	ErFe ₃ (BO ₃) ₄
		[20]	[26]	[22]	[this work]
1	2	3	4	5	
2	0	484	434	404	366
4	0	-1255	-1256	-1192	-1103
4	-3	619	608	554.4	485.4
6	0	404	352	328	309
6	-3	80	73	70.3	58.3
6	6	290	270	232	222
2	-1	39	38	58.4	89.4
4	-1	-76	-66	-49.2	-54.2
6	-1	-32	-27	-7.4	-16.4
2	2	54	54	69.4	67.4
4	2	102	82	101.2	60.2
6	2	-11	-8	-14	-13
4	4	-26	-23	15.9	10.1
6	4	-31	-27	31.4	3.6
6	-5	-131	-91	-79	-70

spin-orbit coupling constant $\zeta = 2368.5$ (2369.6), parameters of two-particle correlation terms $\alpha = 17.67$ (17.8), $\beta = -600$ (-582), $\gamma = 1800$ (1800), parameters of the relativistic spin-other orbit and magnetic spin-dependent interactions $P^2 = 594$, $P^4 = 320$ (297), $P^6 = 60$ (59.4), $M^0 = 3.86$ (3.86), $M^2 = 2.16$ (1.93), $M^4 = 1.2$ (1.29), parameters of three-particle interactions $T^2 = 401$ (400), $T^3 = 43$ (43), $T^4 = 73.8$ (73), $T^6 = -271$ (-271), $T^7 = 298$ (308), $T^8 = 280$ (299); the initial values are in parentheses.

The initial values of the CF parameters were calculated in the framework of the exchange-charge model [27], similarly to our previous studies of crystal fields in RE iron borates [22–26]. Then, they were corrected to achieve minimal differences between the calculated energies of CF levels and the experimental data in column 2 of Table I. The resulting values of CF parameters are given in Table II, together with CF parameters for other RE iron borates having the $P3_121$ crystal structure. The table highlights a systematic change in the trigonal D_3 symmetry parameters' values (the first six lines of Table II) across the RE series. CF parameters of the rhombic C_2 symmetry (the lines 7–14 of Table II) do not show such systematic changes. The matter is that they have little effect on the calculated energies and were taken from the calculations using the exchange-charge model and data on the crystallographic structure, to which they are very sensitive. However, the structural data reported in different works sometimes differ considerably (see, e.g., Refs. [11,16]). Nevertheless, the CF components of rhombic symmetry defined in the five lower lines in the CF Hamiltonian (3) are of paramount importance for understanding some of the physical properties of RE iron borates having the $P3_121$ ($P3_221$) structure, e.g., magnetically nonequivalent positions for RE ions [20], magnetic [22], and quadrupole [21] helix chirality.

The energy levels of Er^{3+} ions found from the analysis of the measured optical spectra and the calculation results

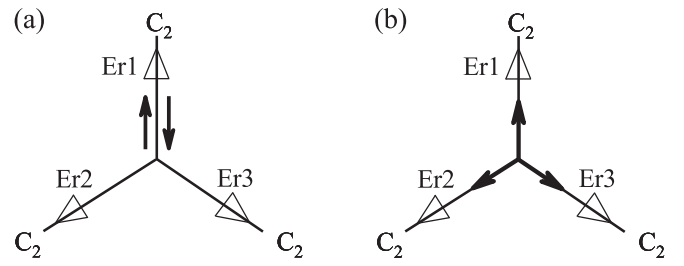


FIG. 7. Arrows show (a) collinear and (b) 120° antiferromagnetic arrangements of the iron magnetic moments. In the case (a), three types of magnetic domains are possible, with Fe magnetic moments along one of the three equivalent C_2 axes in the ab plane. Triangles represent schematically three magnetically nonequivalent Er^{3+} ions characterized by the C_2 point-symmetry group, with their main symmetry axes along the crystalline C_2 axes.

using the CF parameters of Table II are compared in Table I. The root-mean-square difference of 6.23 cm^{-1} between the measured and simulated energies of 43 CF levels (the fourth and fifth sublevels of the ground multiplet $^4I_{15/2}$ have been excluded from the fitting procedure) indicates the reliability of the applied approach. However, the mechanism responsible for the measured in the absorption spectra at elevated temperatures rather large upward shifts of these two fourth and fifth sublevels from the values predicted by the CF model remains unclear.

The obtained wave functions were used to calculate g factors of the ground Kramers doublet (the procedure is described, for instance, in Ref. [34]). The principal axes of the g tensor practically coincide with the crystallographic axes (the a axis is the principal axis by symmetry, the calculated angle between the two other principal axes in the bc -plane and the b and c axes, respectively, equals 1.1°). The corresponding g factors are $g_{aa} = 8.292$ (9.301), $g_{bb} = 10.283$ (9.301), and $g_{cc} = 1.279$ (1.331); in parentheses are the g factors of the impurity Er^{3+} ions in the $\text{YAl}_3(\text{BO}_3)_4$ crystal [36] with the space-symmetry group $R32$. The orbital reduction factor $k = 0.985$ was estimated from the analysis of the magnetic dc susceptibility (see Sec. C below). The single-ion magnetic anisotropy favors an easy-plane magnetic structure in $\text{ErFe}_3(\text{BO}_3)_4$ below T_N .

B. Calculations of the Er^{3+} magnetic moments in a magnetically ordered $\text{ErFe}_3(\text{BO}_3)_4$

The magnetic structure of $\text{ErFe}_3(\text{BO}_3)_4$ was determined from the measurements of powder neutron scattering [11]. According to Ref. [11], the unit cell doubles along the c axis upon transition to the antiferromagnetic phase, with ordering of the Fe^{3+} magnetic moments \mathbf{M}_{Fe} in the ab plane. The moments of the Er^{3+} ions are parallel to the moments of the Fe^{3+} ions and increase from $2.2\mu_B$ at 10 K to $5.3\mu_B$ at $T = 1.5$ K. An additional structure in the erbium sublattice, coexisting with the collinear one, appears at $T = 10$ K—the moments of Er^{3+} ions rotate by 120° in adjacent planes in one-tenth of the crystal volume [11]. Figure 7 illustrates the proposed collinear and 120° phases of iron magnetic moments, under a natural assumption that the Fe moments are oriented along

the C_2 directions in the ab plane. The authors of Ref. [11] associate the appearance of an additional phase with defects in the crystal lattice.

However, the proposed in Ref. [11] magnetic structure contradicts the properties of paramagnetic ions (in this case, the Er^{3+} ions) in a crystal field of the C_2 symmetry. In contrast to the case of the high-temperature $R32$ phase, in the $P3_121$ phase, three Er^{3+} ions in the unit cell are magnetically nonequivalent. For an arbitrary orientation of the collinear magnetic moments of the Fe^{3+} ions in the ab plane, one can expect the appearance of three antiferromagnetically ordered magnetic structures of the Er^{3+} ions with different magnitudes and orientations of their magnetic moments. In particular, if the iron moments \mathbf{M}_{Fe} are oriented along the fixed a axis parallel to one of three equivalent C_2 symmetry axes of the $P3_121$ structure, one can distinguish a subsystem of the Er1 ions with magnetic moments \mathbf{M}_1 parallel to \mathbf{M}_{Fe} and the subsystem of the Er2 ions with their local symmetry axes rotated by the angles $\pm 2\pi/3$ from the a axis and moments \mathbf{M}_2 or \mathbf{M}_2^* which are connected to each other by the 180° rotation around the a axis (see the scheme of Fig. 7). In the framework of this model ($\mathbf{M}_{\text{Fe}} \parallel \mathbf{a}$), we calculated the temperature dependences of components of the Er^{3+} magnetic moments induced by an isotropic exchange interaction with the iron ions. The Hamiltonian of the exchange interaction between the nearest-neighbor erbium and iron ions is written as $H_{\text{exch}} = -2J_{fd}\mathbf{S}_{\text{Fe}}\mathbf{S}_{\text{Er}}$ where J_{fd} is the exchange integral considered as a phenomenological parameter, \mathbf{S}_{Fe} and \mathbf{S}_{Er} are operators of the total spin moments. The value of the exchange integral, $J_{fd} = 0.22 \pm 0.04$ K, used in the present work was obtained from fitting the temperature dependences of the dc susceptibility of $\text{ErFe}_3(\text{BO}_3)_4$ (see Sec. C below), for comparison, in $\text{TbFe}_3(\text{BO}_3)_4$, $J_{fd} = 0.26$ K [26].

There are two different types of iron helical chains along the c axis containing Fe1 and Fe2 ions at Wyckoff sites $3a$ and $6c$ with local C_2 and C_1 symmetry, respectively, in the $P3_121$ ($P3_221$) phase of RE iron borates. RE ions are sixfold coordinated by iron ions, namely by two Fe1 and two pairs of Fe2 ions at the distances of 0.3766 (Fe1), 0.3657, and 0.3835 (Fe2) nm. The effective single-ion Hamiltonian of the Er1 ions in the global Cartesian frame $S(\mathbf{a}, \mathbf{b}, \mathbf{c})$ with the a axis (the C_2 symmetry axis) parallel to the iron magnetic moments $\mathbf{M}_{\text{Fe}\lambda} = -2\mu_{\text{B}}\mathbf{S}_{\text{Fe}\lambda}$ ($\lambda = 1, 2$) in the magnetically ordered phase ($T < T_N$) takes the form

$$H_{\text{Er1}} = H_{\text{FI}} + H_{\text{CF}} \pm 2J_{fd}[M_{\text{Fe1}}(T) + 2M_{\text{Fe2}}(T)]S_{\text{Er},x}/\mu_{\text{B}}. \quad (5)$$

For the Er2 ions, in the local frames $S'(a', b', c)$ rotated by $\pm 2\pi/3$ around the c axis, the corresponding Hamiltonian is written as

$$H_{\text{Er2}} = H_{\text{FI}} + H_{\text{CF}} \pm J_{fd}[M_{\text{Fe1}}(T) + 2M_{\text{Fe2}}(T)](-S_{\text{Er},x} \mp \sqrt{3}S_{\text{Er},y})/\mu_{\text{B}}. \quad (6)$$

Here, we disregard differences between the exchange integrals for Er–Fe1 and Er–Fe2 bonds and neglect long-range magnetic dipolar interactions which are about an order of magnitude weaker than the estimated below exchange interactions between the nearest-neighbor Er^{3+} and Fe^{3+} ions. The

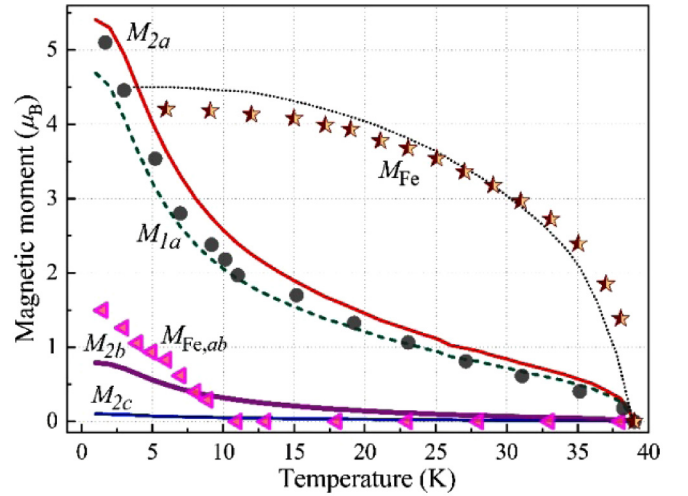


FIG. 8. Measured [11] (symbols) and calculated (lines) magnetic moments of the iron and erbium ions in the antiferromagnetic phase of $\text{ErFe}_3(\text{BO}_3)_4$. Stars and triangles represent the main and additional magnetic structures, respectively, of the iron subsystem with magnetic moments in the ab plane; circles correspond to the erbium magnetic moments collinear to the iron moments in the main structure. The calculated absolute values of the iron and Er1 moments along the a axis are shown by the dotted and dashed lines, respectively; absolute values of projections of the Er2 moments on the a , b , and c axes are shown by solid lines.

temperature dependences of the quantum-statistical expectation values of erbium magnetic moment components in the local frames

$$M_{\lambda,\alpha}(T) = \text{Tr}[\mu_\alpha \exp(-H_{\text{Er}\lambda}/k_{\text{B}}T)]/\text{Tr}[\exp(-H_{\text{Er}\lambda}/k_{\text{B}}T)] \quad (7)$$

(here k_{B} is the Boltzmann constant and $\mu = -\sum_j(kL_j + 2s_j)\mu_{\text{B}}$ is the magnetic moment operator of an erbium ion) depend parametrically on the ordered magnetic moments of the iron ions. Since the temperatures of magnetic phase transitions in isomorphous iron borates $\text{ErFe}_3(\text{BO}_3)_4$ ($T_N = 39$ K) and $\text{YFe}_3(\text{BO}_3)_4$ ($T_N = 38$ K) are almost the same, we used the results of our recent study of helical iron chains in $\text{YFe}_3(\text{BO}_3)_4$ in the framework of a self-consistent four-particle cluster model [37] for describing magnetic properties of the iron subsystem also in $\text{ErFe}_3(\text{BO}_3)_4$. The calculated temperature dependence of the average spontaneous magnetic moment of the iron ions $M_{\text{Fe}} = (M_{\text{Fe1}} + 2M_{\text{Fe2}})/3$ agrees satisfactorily with the neutron magnetic scattering data [11] (see Fig. 8). Next, the magnetic moments \mathbf{M}_1 and \mathbf{M}_2 of Er1 and Er2 ions, respectively, in local systems of coordinates were computed in accordance with Eqs. (5)–(7). The projections of these moments on the axes of the global S frame are shown in Fig. 8.

As follows from the model used, the moments of the Er2 ions are not collinear to the moments of the iron and Er1 ions; they deviate from the a axis by the angles $\pm\varphi$, the magnitude of which increases monotonically and nonlinearly with decreasing temperature up to $\sim 10^\circ$ at $T = 2$ K. As a comparison with the data of Ref. [11] shows, the observed

neutron scattering corresponds to scattering by Er1 and Er2 ions having close in value components of moments along the a axis; additional scattering is associated with the presence of components of the Er2 ion moments parallel to the b axis. This excludes the proposed in Ref. [11] appearance of an additional magnetic structure. It should be noted that the conclusion about the absence of an additional phase at temperatures $T < 10$ K is consistent with the data on the specific heat [38], magnetization [3,38], and optical spectra measurements (Ref. [31] and this work).

C. Magnetic susceptibility of $\text{ErFe}_3(\text{BO}_3)_4$

The temperature dependences of the magnetic susceptibilities of $\text{ErFe}_3(\text{BO}_3)_4$ single crystals for the magnetic fields \mathbf{B} directed along the a , b , and c axes were measured in Ref. [38] and for $\mathbf{B}||c$ and $\mathbf{B}\perp c$ in Refs. [3,11]. We simulated these dependences considering the exchange interaction between erbium and iron ions in the framework of a mean-field approximation. The effective single-ion longitudinal $\chi_{\text{Fe},||}^0 = \chi_{\text{Fe},cc}^0$ and transversal $\chi_{\text{Fe},\perp}^0 = (\chi_{\text{Fe},aa}^0 + \chi_{\text{Fe},bb}^0)/2$ susceptibilities for the Fe^{3+} ions in $\text{YFe}_3(\text{BO}_3)_4$ were computed earlier using the four-particle cluster model in Ref. [37]. For the Er^{3+} ions in weak external magnetic fields \mathbf{B} , we calculated single-ion susceptibilities $\chi_{\text{Er},||}^0 = \chi_{\text{Er},zz}^0$ and $\chi_{\text{Er},\perp}^0 = (\chi_{\text{Er},xx}^0 + \chi_{\text{Er},yy}^0)/2$ using Eqs. (5)–(7) where the Zeeman energy $H_Z = -\mu\mathbf{B}$ was added to the operators (5) and (6). However, local fields contain additional terms corresponding to the exchange f - d interactions. In particular, in the magnetic field parallel to the c axis, when all erbium ions are magnetically equivalent, the local fields at erbium and iron sites are written as $B_{\text{Er},\text{loc}} = B(1 + 3\alpha\chi_{\text{Fe},||})$, $B_{\text{Fe},\text{loc}} = B(1 + \alpha\chi_{\text{Er},||})$, where $\alpha = 2J_{fd}(g_L - 1)/g_L\mu_B^2$ and g_L is the Landé factor for the ground $^4I_{15/2}$ multiplet of Er^{3+} . Using the relations $\chi_{\alpha\beta}^0 B_{\text{loc},\beta} = \chi_{\alpha\beta} B_\beta$, we obtain a system of coupled linear equations for the renormalized single-ion susceptibilities $\chi_{\text{Fe},||}$ and $\chi_{\text{Er},||}$. The final expression for the bulk longitudinal susceptibility (per mole) takes the form

$$\chi_{||} = \frac{N_A(\chi_{\text{Er},||}^0 + 3\chi_{\text{Fe},||}^0 + 6\alpha\chi_{\text{Er},||}^0\chi_{\text{Fe},||}^0)}{1 - 3\alpha^2\chi_{\text{Fe},||}^0\chi_{\text{Er},||}^0}, \quad (8)$$

where N_A is the Avogadro number. For magnetic fields lying in the ab plane, assuming equal probabilities of domains ordered along the three C_2 symmetry axes, we obtain a similar expression

$$\chi_{\perp} = \frac{N_A(\chi_{\text{Er},\perp}^0 + 3\chi_{\text{Fe},\perp}^0 + 6\alpha\chi_{\text{Er},\perp}^0\chi_{\text{Fe},\perp}^0)}{1 - 3\alpha^2\chi_{\text{Fe},\perp}^0\chi_{\text{Er},\perp}^0}. \quad (9)$$

A satisfactory agreement between the calculated and measured susceptibilities (see Fig. 9) was achieved using the values of the two variable parameters, the orbital reduction factor and the exchange integral, $k = 0.985$ and $J_{fd} = 0.22$ K.

To check additionally parameters of the model, we calculated the magnetic-field dependences of the magnetization of $\text{ErFe}_3(\text{BO}_3)_4$ single crystals in the antiferromagnetic phase for magnetic fields $\mathbf{B}||c$ and $\mathbf{B}\perp c$ using the same procedure as the one described above. As is seen in Fig. 10, the results agree satisfactorily with the experimental data [38].

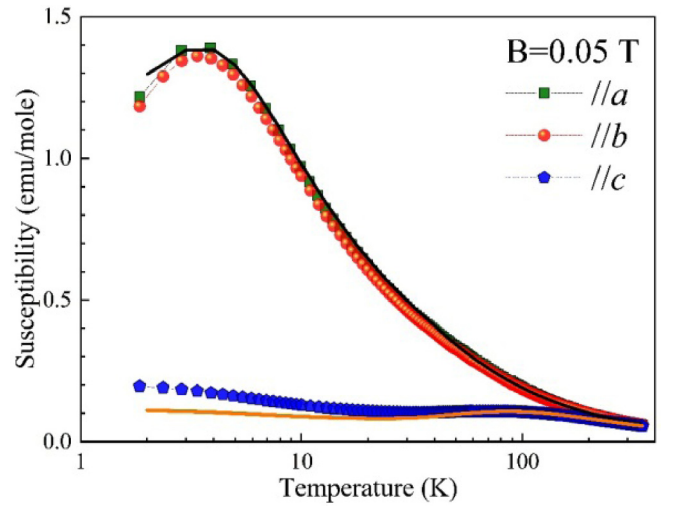


FIG. 9. Static susceptibility in magnetic fields directed along the crystallographic axes of an $\text{ErFe}_3(\text{BO}_3)_4$ crystal. Symbols are experimental data [3,38], solid lines are the results of calculations of the total susceptibility of erbium and iron ions, taking into account the isotropic f - d exchange interaction.

D. Calculations of the Er1 and Er2 spectra in the magnetically ordered $\text{ErFe}_3(\text{BO}_3)_4$

In the framework of the above-discussed model of the iron magnetic structure in a magnetically ordered $\text{ErFe}_3(\text{BO}_3)_4$ ($M_{\text{Fe}}||a$), which was confirmed by a comparison of calculated Er magnetic moments with those measured in neutron-scattering experiments (see Sec. B above), we calculate the positions of the Er1 and Er2 energy levels for $T = 5$ K in the antiferromagnetic phase of $\text{ErFe}_3(\text{BO}_3)_4$, under the assumption of an isotropic Er-Fe exchange interaction. Thus calculated exchange splittings Δ_1 and Δ_2 of Kramers doublets of magnetically nonequivalent Er1 and Er2 at $T = 5$ K are presented in columns 4 and 5 of Table I.

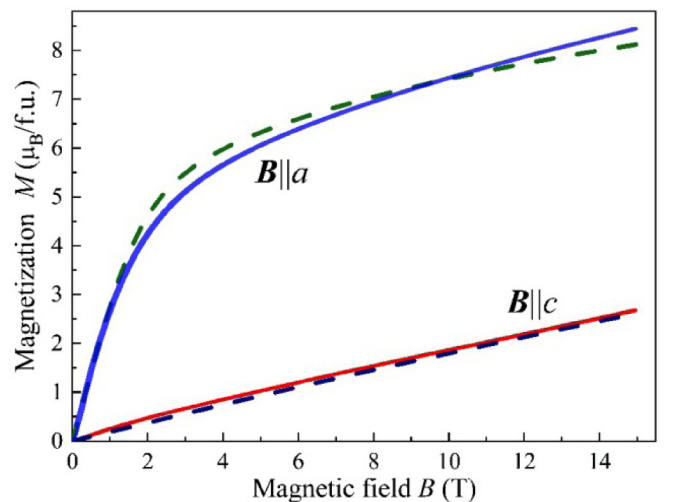


FIG. 10. The measured [38] (solid lines) and calculated (dashed lines) field dependences of the magnetization of $\text{ErFe}_3(\text{BO}_3)_4$ crystal in fields parallel to the crystallographic axes c and a ($T = 4.2$ K).

Each erbium spectral line observed in the paramagnetic phase is split in the general case into eight components in the antiferromagnetic phase, four for Er1 and Er2 (see Fig. 3). In particular, according to calculations, the exchange splitting of the level A in the $^4I_{11/2}$ CF manifold is negligible for both Er1 and Er2 optical centers (about 0.1 cm^{-1} at 5 K) (see Table I) and the contour of the line 1A in the $^4I_{15/2} \rightarrow ^4I_{11/2}$ optical transition should be composed of two components for each of the Er1 and Er2 ions, the integral contribution of Er1 being two times less than that of Er2. Inset of Fig. 6(a) shows a decomposition of the considered line into four Voigt components, one pair of them due to Er2 and the other one (two times less intense)—due to Er1. The experimentally determined ground-state splitting Δ_0 was 5.0 cm^{-1} for Er1 and 7.5 cm^{-1} for Er2, in satisfactory agreement with the calculated values 5.2 and 6.3 cm^{-1} , respectively. A not ideal approximation of the experimental line contour is primarily due to the fact that crystals grown using a $\text{Bi}_2\text{Mo}_3\text{O}_{12}$ -based flux contain unaccounted Er centers near Bi impurities. For this reason, a correct approximation of experimental line contours is not possible. However, we note that for some lines at 5 K up to six maxima or well-defined shoulders are observed (e.g., for the 12414.1 cm^{-1} line) and more than eight components are necessary to approximate the line contour, which is in agreement with the presence of magnetically nonequivalent erbium centers.

V. SUMMARY

In summary, we have performed high-resolution broadband temperature-dependent polarized spectroscopic study of the f - f optical transitions of the Er^{3+} ions in multiferroic $\text{ErFe}_3(\text{BO}_3)_4$ single crystals (space group $P3_121$) in the paramagnetic and antiferromagnetic ($T < T_N = 39 \text{ K}$) phases. From the spectra analysis, positions of 45 CF levels of Er^{3+} (Kramers doublets) in the paramagnetic $\text{ErFe}_3(\text{BO}_3)_4$ ($T = 50 \text{ K}$) were reliably determined. We show that earlier published CF energies [28], based on the analysis of low-resolution spectra of $\text{ErFe}_3(\text{BO}_3)_4$ at $T \geq 90 \text{ K}$, are incorrect, mainly due to a wrong identification of many spectral lines. This wrong identification also resulted in not justified conclusions that crystal fields are different in different electronic states, that the electronic f - f transitions affect local properties

of a crystal, and that the frequencies of local vibrations are different in different excited states of a RE ion.

We use our reliable set of CF levels to calculate the electronic structure of Er^{3+} ions in the crystal field of C_2 symmetry in erbium iron borate. Initial CF parameters were calculated in the frame of the exchange-charge model. Then, they were corrected by comparing the calculated energies of the Er^{3+} CF levels with the experimental optical data. The g factors of the ground Kramers doublet calculated with thus obtained CF parameters reveal the single-ion magnetic anisotropy that favors an easy-plane magnetic structure of $\text{ErFe}_3(\text{BO}_3)_4$ below T_N . What is important, the g tensor is not isotropic in the crystallographic ab plane, because of the low-symmetry (C_2) CF components. This results in three magnetically nonequivalent positions for the Er^{3+} ions in the case of an arbitrary direction of a magnetic field in the ab plane.

Assuming a collinear structure of the iron magnetic moments directed along one of the three equivalent C_2 axes in the ab plane (in this case, there are two magnetically nonequivalent Er systems, Er1 and Er2, with the ratio 1:2) we calculated the temperature dependences of the erbium magnetic moments induced by an isotropic exchange interaction with the iron ions. The results of calculations satisfactorily model the experimentally measured dependences, testifying the adequacy of the theoretical approach used, and explain well the neutron-scattering data [11], without an additional magnetic structure proposed in Ref. [11].

We also calculated the temperature dependences of the longitudinal and transversal magnetic susceptibilities and field dependences of the magnetization in magnetic fields parallel and perpendicular to the crystallographic c axis of the $\text{ErFe}_3(\text{BO}_3)_4$ crystal. The contribution of the iron magnetic system consisting of helical chains directed along the c axis was calculated using a recently developed and tested on $\text{YFe}_3(\text{BO}_3)_4$ self-consistent four-particle cluster model of the Fe^{3+} Heisenberg chains [37], which is a minimal model that quantitatively describes physical properties of high-spin chains. The results of calculations model well the available experimental data.

ACKNOWLEDGMENT

Financial support of the Russian Science Foundation under Grant No. 19-12-00413 is acknowledged.

- [1] A. K. Zvezdin, A. M. Kadomtseva, Yu. F. Popov, G. P. Vorob'ev, A. P. Pyatakov, V. Yu. Ivanov, A. M. Kuz'menko, A. A. Mukhin, L. N. Bezmaternykh, and I. A. Gudim, Magnetic anisotropy and magnetoelectric properties of $\text{Tb}_{1-x}\text{Er}_x\text{Fe}_3(\text{BO}_3)_4$ ferrobates, *Zh. Eksp. Teor. Fiz.* **136**, 80 (2009) [*J. Exp. Theor. Phys.* **109**, 68 (2009)].
- [2] Y. Hinatsu, Y. Doi, K. Ito, M. Wakeshima, and A. Alemi, Magnetic and calorimetric studies on rare-earth iron borates $\text{LnFe}_3(\text{BO}_3)_4$ ($\text{Ln} = \text{Y}, \text{La}-\text{Nd}, \text{Sm}-\text{Ho}$), *J. Solid State Chem.* **172**, 438 (2003).
- [3] A. M. Kadomtseva, Yu. F. Popov, G. P. Vorob'ev, A. P. Pyatakov, S. S. Krotov, K. I. Kamilov, V. Yu. Ivanov, A. A. Mukhin, A. K. Zvezdin, A. M. Kuz'menko, L. N.

Bezmaternykh, I. A. Gudim, and V. L. Temerov, Magnetolectric and magnetoelastic properties of rare-earth ferrobates, *Fiz. Niz. Temp.* **36**, 640 (2010) [*Low Temp. Phys.* **36**, 511 (2010)].

- [4] T. Kurumaji, K. Ohgushi, and Y. Tokura, Magnetolectric responses from the respective magnetic R and Fe subsystems in the noncentrosymmetric antiferromagnets $\text{RFe}_3(\text{BO}_3)_4$ ($R = \text{Eu}, \text{Gd}, \text{and Tb}$), *Phys. Rev. B* **89**, 195126 (2014).
- [5] R. P. Chaudhury, F. Yen, B. Lorenz, Y. Y. Sun, L. N. Bezmaternykh, V. L. Temerov, and C. W. Chu, Magnetolectric effect and spontaneous polarization in $\text{HoFe}_3(\text{BO}_3)_4$ and $\text{Ho}_{0.5}\text{Nd}_{0.5}\text{Fe}_3(\text{BO}_3)_4$, *Phys. Rev. B* **80**, 104424 (2009).

- [6] F. Yen, B. Lorenz, Y. Y. Sun, C. W. Chu, L. N. Bezmaternykh, and A. N. Vasiliev, Magnetic field effect and dielectric anomalies at the spin reorientation phase transition of $\text{GdFe}_3(\text{BO}_3)_4$, *Phys. Rev. B* **73**, 054435 (2006).
- [7] U. Adem, L. Wang, D. Fausti, W. Schottenhamel, P. H. M. van Loosdrecht, A. Vasiliev, L. N. Bezmaternykh, B. Büchner, C. Hess, and R. Klingeler, Magnetodielectric and magnetoelastic coupling in $\text{TbFe}_3(\text{BO}_3)_4$, *Phys. Rev. B* **82**, 064406 (2010).
- [8] A. A. Mukhin, G. P. Vorob'ev, V. Yu. Ivanov, A. M. Kadomtseva, A. S. Narizhnaya, A. M. Kuz'menko, Yu. F. Popov, L. N. Bezmaternykh, and I. A. Gudim, Colossal magnetodielectric effect in $\text{SmFe}_3(\text{BO}_3)_4$ multiferroic, *Pis'ma v Zh. Eksp. Teor. Fiz.* **93**, 305 (2011) [*JETP Lett.* **93**, 275 (2011)].
- [9] M. N. Popova, Optical spectroscopy of low-dimensional rare-earth iron borates, *J. Magn. Magn. Mater.* **321**, 716 (2009).
- [10] M. N. Popova, E. P. Chukalina, T. N. Stanislavchuk, and L. N. Bezmaternykh, Different types of magnetic ordering in $\text{RFe}_3(\text{BO}_3)_4$, $R = \text{Gd, Tb, Er, and Y}$, as studied by the method of Er^{3+} spectroscopic probe, *J. Magn. Magn. Mater.* **300**, e440 (2006).
- [11] C. Ritter, A. Vorotynov, A. Pankrats, G. Petrakovskii, V. Temerov, I. Gudim, and R. Szymczak, Magnetic structure in iron borates $\text{RFe}_3(\text{BO}_3)_4$ ($R = \text{Er, Pr}$): A neutron diffraction and magnetization study, *J. Phys.: Condens. Matter* **22**, 206002 (2010).
- [12] A. I. Popov, D. I. Plokhov, and A. K. Zvezdin, Quantum theory of magnetoelectricity in rare-earth multiferroics: Nd, Sm, and Eu ferrobates, *Phys. Rev. B* **87**, 024413 (2013).
- [13] N. V. Kostyuchenko, A. I. Popov, and A. K. Zvezdin, Features of magnetic and magnetoelectric properties of rare-earth multiferroic $\text{PrFe}_3(\text{BO}_3)_4$ with the singlet ground state, *Fiz. Tverd. Tela* **54**, 1493 (2012) [*Phys. Solid State* **54**, 1591 (2012)].
- [14] N. I. Leonyuk and L. I. Leonyuk, Growth and characterization of $\text{RM}_3(\text{BO}_3)_4$ crystals, *Prog. Cryst. Growth Charact.* **31**, 179 (1995).
- [15] S. A. Klimin, D. Fausti, A. Meetsma, L. N. Bezmaternykh, P. H. M. van Loosdrecht, and T. T. M. Palstra, Evidence for differentiation in the iron-helicoidal chain in $\text{GdFe}_3(\text{BO}_3)_4$, *Acta Crystallogr. Sect. B* **61**, 481 (2005).
- [16] E. S. Smirnova, O. A. Alekseeva, A. P. Dudka, D. N. Khmelenin, K. V. Frolov, M. V. Lyubutina, I. A. Gudim, and I. S. Lyubutin, Crystal structure and structural phase transition in bismuth-containing $\text{HoFe}_3(\text{BO}_3)_4$ in the temperature range 11–500 K, *Acta Crystallogr. Sect. B* **75**, 954 (2019).
- [17] L. N. Bezmaternykh, V. L. Temerov, I. A. Gudim, and N. L. Stolbovaya, Crystallization of trigonal $(\text{Tb, Er})(\text{Fe, Ga})_3(\text{BO}_3)_4$ phases with hantite structure in bismuth trimolybdate-based fluxes, *Crystallogr. Rep.* **50**(Suppl 1), S97 (2005).
- [18] D. Fausti, A. Nugroho, P. H. M. van Loosdrecht, S. A. Klimin, M. N. Popova, and L. N. Bezmaternykh, Raman scattering from phonons and magnons in $\text{RFe}_3(\text{BO}_3)_4$, *Phys. Rev. B* **74**, 024403 (2006).
- [19] A. V. Malakhovskii, A. L. Sukhachev, V. V. Sokolov, T. V. Kutsak, V. S. Bondarev, and I. A. Gudim, Magneto-optical activity of f - f transitions in $\text{ErFe}_3(\text{BO}_3)_4$ and $\text{ErAl}_3(\text{BO}_3)_4$ single crystals, *J. Magn. Magn. Mater.* **384**, 255 (2015).
- [20] M. N. Popova, B. Z. Malkin, K. N. Boldyrev, T. N. Stanislavchuk, D. A. Erofeev, V. L. Temerov, and I. A. Gudim, Evidence for a collinear easy-plane magnetic structure of multiferroic $\text{EuFe}_3(\text{BO}_3)_4$: Spectroscopic and theoretical studies, *Phys. Rev. B* **94**, 184418 (2016).
- [21] T. Usui, Y. Tanaka, H. Nakajima, M. Taguchi, A. Chainani, M. Oura, S. Shin, N. Katayama, H. Sawa, Y. Wakabayashi, and T. Kimura, Observation of quadrupole helix chirality and its domain structure in $\text{DyFe}_3(\text{BO}_3)_4$, *Nat. Mater.* **13**, 611 (2014).
- [22] M. N. Popova, E. P. Chukalina, K. N. Boldyrev, T. N. Stanislavchuk, B. Z. Malkin, and I. A. Gudim, Spectroscopy of f - f transitions, crystal-field calculations, and magnetic and quadrupole helix chirality in $\text{DyFe}_3(\text{BO}_3)_4$, *Phys. Rev. B* **95**, 125131 (2017).
- [23] M. N. Popova, E. P. Chukalina, T. N. Stanislavchuk, B. Z. Malkin, A. R. Zakirov, E. Antic-Fidancev, E. A. Popova, L. N. Bezmaternykh, and V. L. Temerov, Optical spectra, crystal-field parameters, and magnetic susceptibility of multiferroic $\text{NdFe}_3(\text{BO}_3)_4$, *Phys. Rev. B* **75**, 224435 (2007).
- [24] M. N. Popova, E. P. Chukalina, B. Z. Malkin, D. A. Erofeev, L. N. Bezmaternykh, and I. A. Gudim, Crystal field and exchange interactions in the $\text{SmFe}_3(\text{BO}_3)_4$ multiferroic, *Zh. Eksp. Teor. Fiz.* **145**, 128 (2014) [*J. Exp. Theor. Phys.* **118**, 111 (2014)].
- [25] M. N. Popova, T. N. Stanislavchuk, B. Z. Malkin, and L. N. Bezmaternykh, Optical spectroscopy of $\text{PrFe}_3(\text{BO}_3)_4$: Crystal-field and anisotropic Pr-Fe exchange interactions, *Phys. Rev. B* **80**, 195101 (2009).
- [26] M. N. Popova, T. N. Stanislavchuk, B. Z. Malkin, and L. N. Bezmaternykh, Phase transitions and crystal-field and exchange interactions in $\text{TbFe}_3(\text{BO}_3)_4$ as seen via optical spectroscopy, *J. Phys.: Condens. Matter* **24**, 196002 (2012).
- [27] B. Z. Malkin, Crystal field and electron-phonon interaction in rare-earth ionic paramagnets, in *Spectroscopy of Solids Containing Rare Earth Ions*, edited by A. A. Kaplyanskii and R. M. Macfarlane (North Holland, Amsterdam, The Netherlands, 1987), Vol. 21, pp.13–50.
- [28] A. V. Malakhovskii, V. V. Sokolov, and I. A. Gudim, Influence of the low local symmetry of Er^{3+} ions on magnetic circular dichroism and absorption spectra of f - f transitions in $\text{ErFe}_3(\text{BO}_3)_4$ single crystal, *J. Magn. Magn. Mater.* **465**, 700 (2018).
- [29] I. A. Gudim, E. V. Eremin, and V. L. Temerov, Flux growth and spin reorientation in trigonal $\text{Nd}_{1-x}\text{Dy}_x\text{Fe}_3(\text{BO}_3)_4$ single crystals, *J. Crystal Growth* **312**, 2427 (2010).
- [30] A. M. Kalashnikova, V. V. Pavlov, R. V. Pisarev, L. N. Bezmaternykh, M. Bayer, and Th. Rasing, Linear and nonlinear optical spectroscopy of gadolinium iron borate $\text{GdFe}_3(\text{BO}_3)_4$, *Pis'ma v Zh. Eksp. Teor. Fiz.* **80**, 339 (2004) [*JETP Lett.* **80**, 293 (2004)].
- [31] D. Erofeev, A. Jablunovskis, and E. Chukalina, Optical spectroscopy of $\text{ErFe}_3(\text{BO}_3)_4$: Detection of phase transitions and crystal-field levels of the Er^{3+} ground multiplet, *EPJ Web of Conferences* **185**, 07002 (2018).
- [32] W. T. Carnall, G. L. Goodman, K. Rajnak, and R. S. Rana, A systematic analysis of the spectra of the lanthanides doped into single crystal LaF_3 , *J. Chem. Phys.* **90**, 3443 (1989).
- [33] O. K. Moune, D. Garcia, and M. D. Faucher, Improvement of the parametric simulation of energy levels in erbium compounds, *J. Phys. Chem. Sol.* **52**, 513 (1991).
- [34] B. Z. Malkin, S. I. Nikitin, R. V. Yusupov, I. F. Gilmutdinov, I. E. Mumdzhi, R. Batulin, A. G. Kiiamov, D. G. Zverev, B. F. Gabbasov, O. A. Petrenko, O. Young, and D. T. Androja,

- Magnetic and spectral properties of the multisublattice oxides $\text{SrY}_2\text{O}_4 : \text{Er}^{3+}$ and SrEr_2O_4 , *Phys. Rev. B* **92**, 094415 (2015).
- [35] A. Baraldi, R. Capelletti, N. Magnani, M. Mazzera, E. Beregi, and I. Foldvari, Spectroscopic investigation and crystal field modelling of Dy^{3+} and Er^{3+} energy levels in yttrium aluminium borate (YAB) single crystals, *J. Phys.: Condens. Matter* **17**, 6245 (2005).
- [36] A. D. Prokhorov, A. A. Prokhorov, L. F. Chernysh, P. Aleshkevich, V. Dyakonov, and H. Szymczak, EPR of Nd^{3+} and Er^{3+} ions in aluminum borates $\text{YAl}_3(\text{BO}_3)_4$ and $\text{EuAl}_3(\text{BO}_3)_4$, *J. Magn. Magn. Mater.* **326**, 162 (2013).
- [37] B. Z. Malkin, E. A. Popova, E. P. Chukalina, A. Jablunovskis, and M. N. Popova, Self-consistent four-particle cluster model of Fe^{3+} heisenberg chains: Spectral and magnetic properties of $\text{YFe}_3(\text{BO}_3)_4$ crystals, *phys. status solidi–Rapid Res. Lett.* **14**, 1900603 (2020).
- [38] E. A. Popova, A. N. Vasiliev, V. L. Temerov, L. N. Bezmaternykh, N. Tristan, R. Klingeler, and B. Büchner, Magnetic and specific heat properties of $\text{YFe}_3(\text{BO}_3)_4$ and $\text{ErFe}_3(\text{BO}_3)_4$, *J. Phys.: Condens. Matter* **22**, 116006 (2010).